

高功率光纤激光深熔焊接飞溅特性以及离焦量对飞溅的影响

张高磊, 孔华, 邹江林*, 赵振家, 肖荣诗

北京工业大学材料与制造学部高功率及超快激光先进制造实验室, 北京 100124

摘要 飞溅是激光深熔焊接中最严重的缺陷之一。本文通过熔池原位光学观察和板材质量亏损计算,研究了高功率光纤激光深熔焊接过程中的飞溅行为以及离焦量对飞溅的影响。结果表明:飞溅的形成可分为三步,熔池凸起→凸起部位拉长形成液体柱→液体柱克服表面张力断裂形成飞溅;飞溅的直径主要分布在 $>50\sim 100\ \mu\text{m}$ 之间;随着离焦量增加,飞溅数量、板材质量亏损和熔宽均逐渐增加,熔深则逐渐减小。进一步分析结果表明:飞溅的喷发与小孔前壁倾斜角、小孔前壁激光致蒸发蒸气的冲击力、熔池表面张力有关;增加离焦量会减小前壁的倾斜角和熔池表面张力,同时增加前壁的激光致蒸发蒸气对小孔后壁上沿的冲击效果,使飞溅更易于产生。

关键词 激光技术; 飞溅; 熔池; 蒸气; 离焦量; 小孔前壁

中图分类号 TG456.7

文献标志码 A

doi: 10.3788/CJL202148.2202008

1 引言

高功率光纤激光与 CO_2 激光、Nd:YAG 激光、碟片激光相比,具有加工柔性高、功率高、光束质量好和运行成本低等优势^[1-5],但其在深熔焊接过程中极易产生大量飞溅颗粒,对焊接过程产生严重的负面影响^[6-10]。一方面,飞溅会污染聚焦镜或存在于光束传输路径中,导致激光束聚焦特性改变或激光传输能量损失,严重影响焊接过程的稳定性;另一方面,飞溅会导致焊缝金属亏损,产生凹陷、焊缝未填满等焊接缺陷,严重影响焊接接头的完整性和焊接构件的整体服役性能。因此,研究飞溅的产生对理解光纤激光深熔焊接物理过程及优化焊接工艺技术具有重要意义。

近年来,已有大量研究关注于激光深熔焊接中飞溅的形成过程^[11-24]。Kaplan 等^[16]指出,在激光焊接过程中,当熔池中液滴的动能足以克服熔池表面的张力能时,液滴将会飞出熔池表面形成飞溅颗粒。Li 等^[17]认为不同的焊接参数会导致不同的熔

池流形,故而会影响焊接飞溅的形成。Heider 等^[18]认为在激光焊接铜过程中,深熔小孔底部尖端气泡生长至爆炸是形成焊接飞溅的关键因素。Wu 等^[19]指出,随着深熔小孔口尺寸减小,小孔口前沿凸起的液体柱逐渐拉长并断裂是形成飞溅的原因。Kawahito 等^[20]认为小孔内激光诱导羽辉作用于小孔后壁的强剪切力是推动熔池形成飞溅的主要原因。Zhang 等^[21]认为飞溅的产生与小孔前壁激光致蒸发反冲压力对前壁熔化层的挤压以及蒸气对小孔后壁熔池的冲击有关。Chang 等^[22]认为激光焊接铝合金过程中影响飞溅的主要因素是激光功率密度。

在高功率光纤激光焊接低碳钢过程中,本研发团队采用高速摄像机对飞溅的形成过程以及熔池的波动行为进行观察。焊接结束后,利用扫描电镜对收集的飞溅进行尺寸测量和数量统计,并计算板材的质量亏损。通过变化离焦量的方式改变光纤激光的功率密度,研究不同离焦量下飞溅的数量和板材的质量亏损。最后综合试验结果分析离焦量对板材质量亏损和飞溅形成的影响规律。

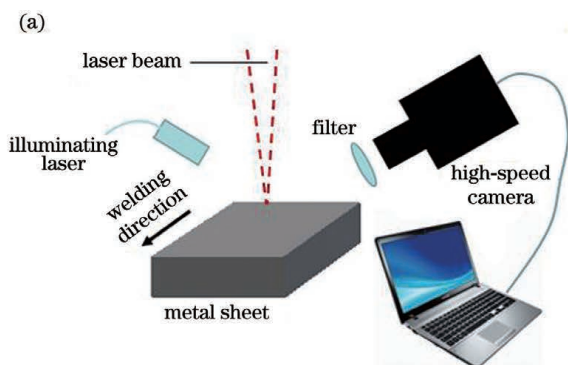
收稿日期: 2021-05-11; 修回日期: 2021-05-26; 录用日期: 2021-06-02

基金项目: 国家自然科学基金面上项目(51875007)、国家重点研发计划(2018YFB1107801)

通信作者: *zoujianglin1@163.com

2 试验方法

采用 IPG 公司生产的 YLS-6000 光纤激光器进行焊接试验,该激光器发射激光的波长为 $1.07\ \mu\text{m}$,额定输出功率为 6 kW。激光束经过芯径为 $200\ \mu\text{m}$



的光纤传输,输出耦合准直镜的焦距为 200 mm。聚焦镜的焦距为 300 mm,光束经聚焦后的焦点直径为 $0.31\ \text{mm}$,瑞利长度为 $3.07\ \text{mm}$ 。试验过程中激光器的输出功率固定为 6 kW,焊接速度为 $3\ \text{m}/\text{min}$ 。试验布置示意图如图 1(a)所示。

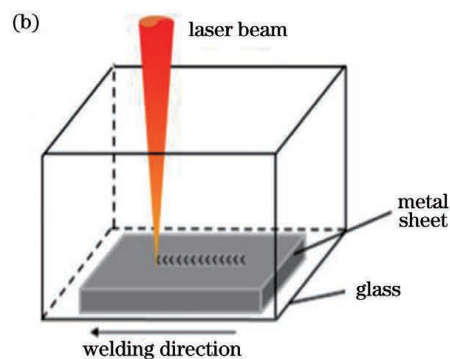


图 1 试验装置示意图。(a)观察飞溅和熔池;(b)飞溅收集装置

Fig. 1 Experimental device diagrams. (a) Observation of spatters and molten pool; (b) spatter collection device

采用 PHOTRON Fastcam Mini UX100 彩色高速摄像仪对焊接过程中的熔池形态以及飞溅的形成过程进行拍摄。高速摄像仪的采集帧数设置为 $10000\ \text{frame}/\text{s}$,试验中高速摄像仪的镜头与焊接板面间呈 45° 角。此外,利用波长为 $808\ \text{nm}$ 、功率为 $50\ \text{W}$ 的半导体激光作为照明光源辐照焊接熔池。高速摄像仪配备中心波段为 $808\ \text{nm}$ 的窄带滤波片。为了统计飞溅的尺寸分布,采用玻璃缸收集焊接过程中产生的飞溅,如图 1(b)所示。焊接结束后,采用 JSM-6510 型扫描电镜对收集的飞溅进行形貌观察和数量统计。

焊接材料为低碳钢,其尺寸为 $100\ \text{mm} \times 20\ \text{mm} \times 10\ \text{mm}$,化学成分(质量分数)为: $99.5\% \text{Fe}$, $0.3\% \text{C}$ 。将待焊表面进行磨削处理,焊前用丙酮清洗干净。采用 JJ324BC 高精度天平(精度为

$\pm 0.2\ \text{mg}$)测量焊接前后板材的质量,将其差值除以焊缝长度就可以得到板材质量的亏损。每个参数下的试样重复测量三次,质量亏损取 3 次测量的平均值。最后从每个工艺参数下的 1000 帧高速摄像中获取 $100\ \text{ms}$ 内的飞溅数量,然后乘 10 即可得到每秒产生的飞溅数量。飞溅数量也取 3 次测量的平均值。焊后沿焊缝中心切割焊缝,焊缝横截面经过抛光、腐蚀后,用 Keyence VHX950 光学显微镜测量其熔深和熔宽。

3 试验结果

3.1 飞溅的特性

在 $3\ \text{m}/\text{min}$ 焊接速度下进行零离焦焊接,采用高速摄像仪对光纤激光深熔焊接过程进行观察,获得典型的飞溅颗粒的形成过程,结果如图 2 所示。

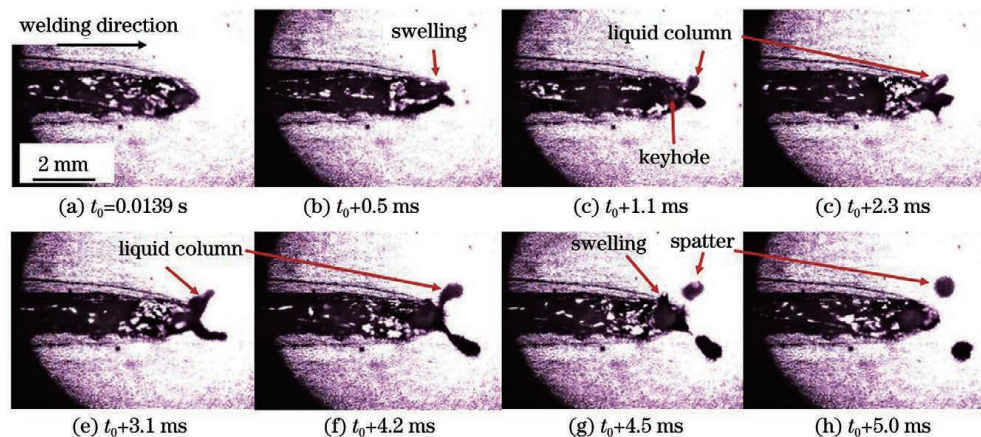


图 2 飞溅颗粒的形成过程

Fig. 2 Formation process of spatter particles

可见,熔池呈狭长形,其表面形态不规则,飞溅颗粒产生于小孔口的边沿。小孔口边沿的熔体受到挤压形成液柱(如图 2 中的 $t_0 + 0.5 \text{ ms}$ 至 $t_0 + 4.2 \text{ ms}$),随后液柱断裂形成飞溅颗粒(如图 2 中的 $t_0 + 4.5 \text{ ms}$)。飞溅的形成过程可归结为:孔口边沿熔池凸起→凸起部位拉长形成液体柱→液体柱克服表面张力断裂形成飞溅颗粒。飞溅颗粒基本呈球状,如图 2(h)所示。

焊接结束后,采用扫描电镜观察玻璃缸内收集的飞溅颗粒(某一条焊缝成形过程中产生的飞溅颗粒)的形貌,其形貌近似呈球形,直径差异较大。所有飞溅颗粒尺寸的概率分布如图 3 所示,可见:直径在 $1 \sim 50 \mu\text{m}$ 区间的飞溅颗粒在所有颗粒中的占比约为 29%(由于更小直径的微粒在收集过程中也更容易遗失,故而该值可能偏小);直径在 $>50 \sim 100 \mu\text{m}$ 区间的飞溅颗粒的占比约为 50%;直径在 $>100 \sim 150 \mu\text{m}$ 区间的飞溅颗粒的占比约为 15%;其他尺寸的飞溅颗粒的占比低于 6%。该结果表明光纤激光深熔焊接飞溅颗粒的尺寸分布在 $1 \sim 150 \mu\text{m}$ 之间,且主要分布在 $>50 \sim 100 \mu\text{m}$ 之间。

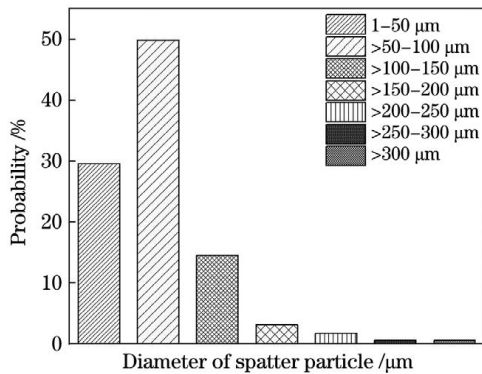


图 3 飞溅颗粒尺寸的概率分布

Fig. 3 Probability distribution of spatter particle size

3.2 离焦量对板材质量亏损及飞溅数量的影响

图 4 为不同离焦下焊接羽辉的形貌特征和飞溅的喷发情况。可以发现,狭长的羽辉类似于激光束的聚焦形态,其高度可超过 40 mm,并呈现出不连续的特征。狭长形羽辉的周围存在大量飞溅。离焦量为 0 mm 时,狭长形羽辉最暗且最狭小,飞溅量也相对最少。随着离焦量增加,羽辉面积逐渐增大,且亮度逐渐增强,飞溅量也明显增多。该现象表明,增加离焦量能使羽辉强度显著增强,飞溅量明显增多。

图 5 为不同离焦量下熔池的形貌特征和飞溅的喷发情况。可见:离焦量为 0 mm 时,熔池的波动相对稳定,板材表面上存在相对少的飞溅颗粒;随着

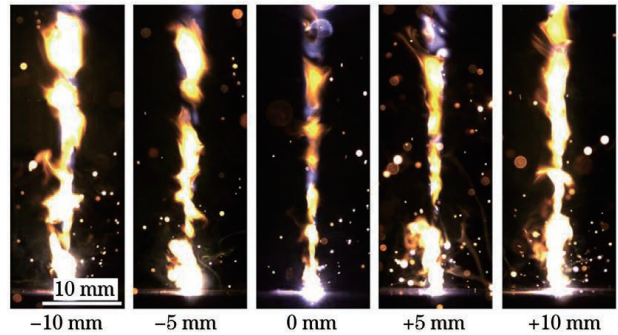


图 4 羽辉和飞溅喷发特征随离焦量的变化规律

Fig. 4 Variations of plume and spatters characteristics with defocus

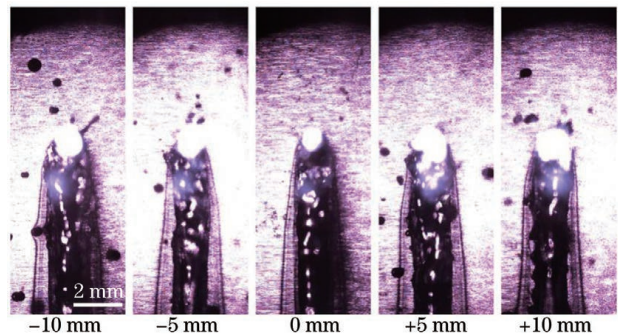


图 5 熔池形貌与离焦量之间的关系

Fig. 5 Relationship between molten pool and defocus

正/负离焦量增大,焊接过程变得不稳定,附着于板材表面的飞溅更多、更大。正/负离焦的变化对飞溅、熔池表面形态的影响基本是一致的。

图 6 为焊接板材的质量亏损和飞溅数量随离焦量的变化规律。可见:零离焦焊接时,板材的质量亏损和飞溅数量最少,平均质量亏损约为 0.73 mg/mm ,每秒飞溅数量约为 550 个;随着正/负离焦量增加,焊接板材的质量亏损及飞溅数量均增加;-10 mm 离焦量与 +10 mm 离焦量下的质量亏损几乎相同,

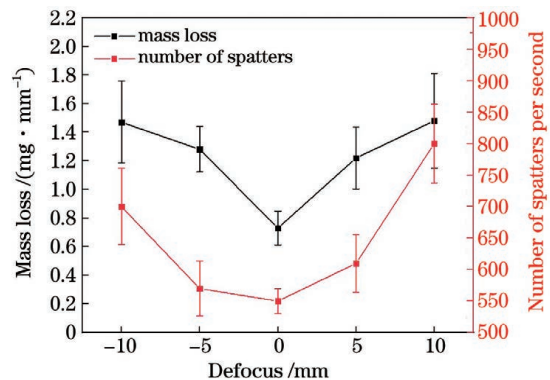


图 6 板材质量亏损、飞溅数量随离焦量的变化规律

Fig. 6 Variations of plate mass loss and number of spatters with defocus

约为 1.46 mg/mm; -10 mm 离焦量下的每秒飞溅数量约为 700 个, +10 mm 离焦量下的每秒飞溅数量约为 790 个。由此可见, 激光功率不变时, 飞溅数量、板材质量亏损均与离焦量呈正相关关系。这表明采用飞溅数量或焊接板材质量亏损均可表征焊接过程中飞溅喷发的激烈程度。此外, 随着离焦量增加, 三处测量数据之间的差异性逐渐增大, 说明大离焦焊接条件下的焊接过程不稳定。

此外, 由图 6 还可以看出, 正离焦时的飞溅数量明显较负离焦时多, 而正负离焦时板材的质量亏损却几乎相同。造成该差异的原因可能是负离焦时焦点位于小孔内(板面下方), 激光致小孔孔壁蒸发相比正离焦时更剧烈, 故而产生的飞溅颗粒尺寸更大, 导致板材的质量亏损变大。

3.3 离焦量对小孔前壁倾斜角的影响

图 7 是小孔口直径(沿焊接方向上的孔口直径)、熔深、熔宽随离焦量的变化规律。当离焦量为 0 mm 时, 小孔口直径约为 1.2 mm, 熔深约为 6.1 mm, 熔宽约为 1.8 mm; 随着离焦量增加, 小孔口直径和熔宽均呈现递增的趋势, 而熔深却呈现出逐渐减小的趋势; 当离焦量增至 +10 mm 时, 小孔口直径增至约 1.5 mm, 熔宽增至 2.3 mm, 熔深则减小至约为 4.2 mm。随着负离焦量的增加, 小孔口直径、熔深和熔宽均呈现出与正离焦相似的变化规律。由此可见, 随着离焦量变化, 小孔口直径和熔宽均与离焦量呈正相关关系, 与图 6 中所呈现出的飞溅数量、板材质量亏损与离焦量的关系一致。此外, 熔深与离焦量呈负相关关系。

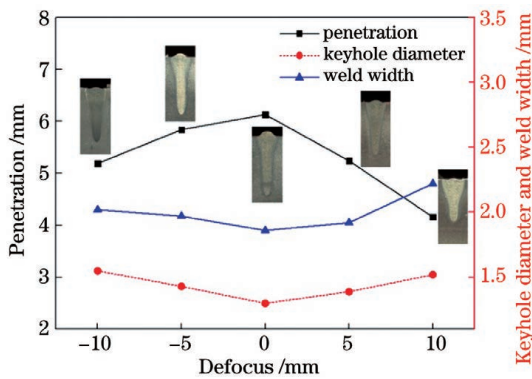


图 7 熔深、熔宽和小孔口直径随离焦量的变化规律
Fig. 7 Variations of penetration, weld width, and keyhole diameter with defocus

熔深和深熔小孔口半径(沿焊接方向上的半径)的比值近似为小孔前壁倾斜角的正切值, 利用该值可以近似计算出小孔前壁的倾斜角, 如图 8 所示。

利用图 7 中熔深和小孔口半径的数值, 可以近似计算得到小孔前壁倾斜角随离焦量的变化规律, 计算结果如图 9 所示。离焦量越小(光斑直径越小), 小孔前壁的倾斜角越陡峭, 离焦量为 0 时倾斜角约为 84°; 随着离焦量增加, 小孔前壁的倾斜角逐渐减小, +10 mm 离焦时减小到约为 80°。小孔前壁倾斜角随正离焦增大而减小的幅度略大于负离焦, 这也可能是飞溅数量在正离焦时相对于负离焦较多的原因。

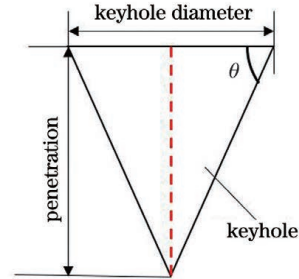


图 8 小孔前壁倾斜角计算示意图

Fig. 8 Schematic of calculating the inclination angle of the front keyhole wall

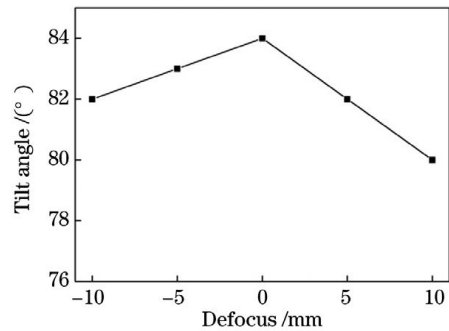


图 9 小孔前壁倾斜角随离焦量的变化规律

Fig. 9 Variation of tilt angle of the front keyhole wall with the defocus

4 分析与讨论

在高功率光纤激光深熔焊接过程中, 激光束直接辐照小孔前壁, 小孔前壁对入射激光的第一次吸收决定了小孔的深度^[23]。Fabbro 等^[24]认为小孔前壁对入射激光的第一次吸收在 60%~80% 之间。Zou 等^[25-26]认为小孔前壁表面是粗糙的。根据小孔前壁对入射激光的一次吸收较高以及粗糙曲面对入射激光的漫反射效应, 可推测出前壁的反射光较弱, 该反射光作用于小孔后壁时对熔池的影响较小。因此, 在光纤激光深熔焊接过程中对小孔孔壁(熔池)扰动的力是小孔前壁的激光致蒸发反冲压力以及激光致蒸发蒸气对小孔后壁的冲击力^[27]。

小孔前壁的激光致蒸发反冲压力以及激光致蒸

发蒸气对小孔后壁的冲击力使作用位置处的熔体受力不均,从而在熔池表面凸起。凸起部分的熔体的动能满足(1)式所示的条件即可形成飞溅^[16]。

$$\rho_m v_m^2 > \frac{2\sigma}{r}, \quad (1)$$

式中: σ 为熔池表面的张力系数; r 为熔池凸起部分的半径; ρ_m 为熔体的密度; v_m 为熔池表面熔体向外凸起的流动速度。在稳定状态下,前壁表面的熔体近似以光斑中心为起点向光斑径向方向流动,利用伯努利方程可以得到熔池表面熔体向外凸起的流动速度 v_m 与轴线上其他位置处的反冲压力 p_r 之间的关系^[28],即

$$p_r = \frac{\rho_m v_m^2}{2}. \quad (2)$$

结合(1)式和(2)式可得

$$p_r > \frac{\sigma}{r}. \quad (3)$$

当凸起的熔体柱满足(3)式时,即可断裂产生飞溅。由此可见,熔池中飞溅的喷发是小孔前壁激光致蒸发反冲压力、激光致蒸发蒸气对小孔后壁的冲击力以及熔池表面张力共同作用的结果。

小孔前壁表面的蒸发反冲压力与其法线方向相反,该蒸气对小孔后壁冲击力的方向与前壁表面法线方向相同^[29],如图 10 所示。即:小孔前壁表面激光致蒸发反冲压力与激光致蒸发蒸气对小孔后壁冲击力的方向均在前壁表面的法线方向上,并随着前壁表面法线的改变而变化。在光纤激光深熔焊接过程中,根据飞溅的喷发位置可将飞溅大致分为小孔口前部喷发的飞溅和小孔口后部喷发的飞溅。小孔前壁表面蒸发反冲压力挤压前壁上的熔化层是小孔口前部飞溅形成的原因,沿前壁表面法线方向喷发的激光致蒸气冲击小孔后壁是小孔口后部飞溅形成的原因^[27]。

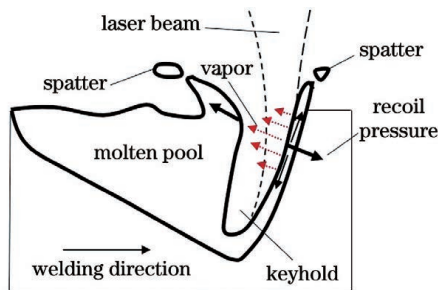


图 10 金属蒸气与飞溅之间的关系

Fig. 10 Relationship between metal vapor and spatter

根据图 9,离焦量越大,小孔前壁的倾斜角越小,且越接近金属铁在沸点温度时的布儒斯特角(约

80°^[30])。前壁倾斜角减小并接近布儒斯特角会导致两种结果:1)随着前壁对入射激光的吸收增大,激光致蒸发反冲压力和激光致蒸发蒸气对小孔后壁的冲击力均增大,这将导致更多的飞溅产生;2)随着小孔前壁的倾斜角减小,源自前壁的蒸发蒸气对小孔后壁的力学冲击方向将变为斜向上(后壁的熔池体积大),这将更有利于蒸气冲击小孔后部熔池,从而产生飞溅。这两方面均说明光纤激光深熔焊接飞溅随着离焦量的增大而增多。

由图 4 可发现,在光纤激光深熔焊接过程中,类似于激光束聚焦形态的狭长形羽辉随着离焦量的增加而增强。韩雪等^[31]指出其原因与激光加热光束内的微粒有关。光纤激光深熔焊接时,光束内的微粒会对光的传输产生严重的负面影响^[32]。在变离焦量焊接中,光斑直径的增大一方面会导致激光功率密度降低,光束内的微粒不易气化消失,使得微粒对激光束的传输产生更长时间的负面作用;另一方面,微粒进入激光束内的概率增大,从而对焊接过程产生的负面影响越严重。无论是哪一种情况,均可以确定增加离焦量焊接时光束中的微粒会进一步恶化光束的传输,从而影响小孔前壁表面激光致蒸气在作用区域的空间分布,导致熔池的稳定性发生恶化。这是焊接过程的稳定性随着离焦量的增大而恶化,更易产生飞溅的另外一个原因。

根据(1)式,表面张力系数越小,熔池在相同外界驱动力作用下越易形成飞溅。离焦量越大,熔池(熔宽)就越宽,从激光作用位置(小孔口)的高温区域至焊缝边沿(熔点)的温度梯度就越小。由此可以推测出:离焦量越大,小孔口附近高温区的面积就越大。由于熔体的表面张力系数与其温度呈负相关关系,故而该区域对应的表面张力越小,在相同的驱动力下越容易形成飞溅。这是随着离焦量增加,飞溅喷发越剧烈的另外一个原因。总之,离焦量增加将使小孔前壁倾斜角减小(接近布儒斯特角时,激光致蒸发蒸气的冲击力增加,其喷发方向更有利于后部熔池形成飞溅)、光束内微粒对激光的扰动增加、熔池表面张力减小(熔池变宽),这三方面因素均有利于飞溅喷发的增强以及焊接板材质量亏损的增加。

5 结 论

飞溅的形成过程为:孔口边沿熔池凸起→凸起部位拉长形成液体柱→液体柱克服表面张力断裂形成飞溅。飞溅颗粒的直径主要分布在 $>50 \sim 100 \mu\text{m}$ 之间。

飞溅数量和焊接板材的质量亏损均可表征焊接过程中飞溅喷发的剧烈程度;飞溅数量、焊接板材质量亏损、熔宽与离焦量呈正相关关系,熔深与离焦量呈负相关关系。

飞溅的喷发与小孔前壁倾斜角、小孔前壁激光致蒸发蒸气的冲击力、熔池表面张力有关;增加离焦量将减小前壁的倾斜角和孔口附近区域熔池的表面张力,同时增加源自前壁的蒸发蒸气对小孔后壁上沿的力学冲击效果,这三方面因素均有利于飞溅的产生。

参 考 文 献

- [1] Zhao L, Cao Z, Zou J L, et al. Keyhole morphological characteristics in high-power deep penetration fiber laser welding[J]. Chinese Journal of Lasers, 2020, 47(11): 1102005.
赵乐, 曹政, 邹江林, 等. 高功率光纤激光深熔焊接小孔的形貌特征[J]. 中国激光, 2020, 47(11): 1102005.
- [2] Xu G J, Li X, Hang Z X, et al. Laser welding of high strength steel using fiber laser and CO₂ laser[J]. Laser & Optoelectronics Progress, 2014, 51(3): 031403.
徐国建, 李响, 杭争翔, 等. 光纤激光及CO₂激光焊接高强钢[J]. 激光与光电子学进展, 2014, 51(3): 031403.
- [3] Zou J L, Wu S K, Xiao R S, et al. Comparison of melting efficiency in high power fiber laser and CO₂ laser welding[J]. Chinese Journal of Lasers, 2013, 40(8): 0803002.
邹江林, 吴世凯, 肖荣诗, 等. 高功率光纤激光和CO₂激光焊接熔化效率对比[J]. 中国激光, 2013, 40(8): 0803002.
- [4] Zou J L, Li F, Niu J Q, et al. Effect of laser-induced plume on welding process during high power fiber laser welding[J]. Chinese Journal of Lasers, 2014, 41(6): 0603005.
邹江林, 李飞, 牛建强, 等. 高功率光纤激光焊接羽辉对焊接过程的影响[J]. 中国激光, 2014, 41(6): 0603005.
- [5] Zhang M J. Study on the behavior of metallic vapor plume and defects control during deep penetration laser welding of thick plate using 10-kW level high power fiber laser[D]. Changsha: Hunan University, 2013.
张明军. 万瓦级光纤激光深熔焊接厚板金属蒸气行为与缺陷控制[D]. 长沙: 湖南大学, 2013.
- [6] Cai H, Xiao R S. Statistic analysis on spatter characteristics in high power CO₂ laser and fiber laser welding of thin sheet aluminum alloy[J]. Transactions of the China Welding Institution, 2013, 34(2): 27-30, 114.
蔡华, 肖荣诗. 薄板铝合金高功率CO₂激光与光纤激光焊接飞溅特性对比分析[J]. 焊接学报, 2013, 34(2): 27-30, 114.
- [7] Schmidt L, Schrickler K, Bergmann J P, et al. Effect of local gas flow in full penetration laser beam welding with high welding speeds[J]. Applied Sciences, 2020, 10(5): 1867.
- [8] Rominger V, Berger P, Hügel H. Effects of reduced ambient pressure on spattering during the laser beam welding of mild steel[J]. Journal of Laser Applications, 2019, 31(4): 042016.
- [9] Li S C, Chen G, Zhang M J, et al. Dynamic keyhole profile during high-power deep-penetration laser welding[J]. Journal of Materials Processing Technology, 2014, 214(3): 565-570.
- [10] Zhang D B, Li C L, Liu X X, et al. Numerical study of spatter formation during fiber laser welding of aluminum alloy[J]. Journal of Manufacturing Processes, 2018, 31: 72-79.
- [11] Zhao C, Guo Q L, Li X X, et al. Bulk-explosion-induced metal spattering during laser processing[J]. Physical Review X, 2019, 9(2): 021052.
- [12] Huang Y, Hua X M, Li F, et al. Spatter feature analysis in laser welding based on motion tracking method[J]. Journal of Manufacturing Processes, 2020, 55: 220-229.
- [13] Li X Y, Li F, Hua X M, et al. Analysis of back-weld spatters in laser welding of CP-Ti[J]. Journal of Manufacturing Processes, 2020, 53: 48-54.
- [14] Nakamura H, Kawahito Y, Nishimoto K, et al. Elucidation of melt flows and spatter formation mechanisms during high power laser welding of pure titanium[J]. Journal of Laser Applications, 2015, 27(3): 032012.
- [15] Miyagi M, Zhang X D. Investigation of laser welding phenomena of pure copper by X-ray observation system[J]. Journal of Laser Applications, 2015, 27(4): 042005.
- [16] Kaplan A F H, Powell J. Spatter in laser welding[J]. Journal of Laser Applications, 2011, 23(3): 032005.
- [17] Li S C, Chen G Y, Katayama S, et al. Relationship between spatter formation and dynamic molten pool during high-power deep-penetration laser welding[J]. Applied Surface Science, 2014, 303: 481-488.
- [18] Heider A, Sollinger J, Abt F, et al. High-speed X-ray analysis of spatter formation in laser welding of copper[J]. Physics Procedia, 2013, 41: 112-118.
- [19] Wu D S, Hua X M, Huang L J, et al. Observation

- of the keyhole behavior, spatter, and keyhole-induced bubble formation in laser welding of a steel/glass sandwich[J]. *Welding in the World*, 2019, 63(3): 815-823.
- [20] Kawahito Y, Mizutani M, Katayama S. High quality welding of stainless steel with 10 kW high power fibre laser[J]. *Science and Technology of Welding and Joining*, 2009, 14(4): 288-294.
- [21] Zhang M J, Chen G Y, Zhou Y, et al. Observation of spatter formation mechanisms in high-power fiber laser welding of thick plate [J]. *Applied Surface Science*, 2013, 280: 868-875.
- [22] Chang B H, Blackburn J, Allen C, et al. Studies on the spatter behaviour when welding AA5083 with a Yb-fibre laser[J]. *The International Journal of Advanced Manufacturing Technology*, 2016, 84(9/10/11/12): 1769-1776.
- [23] Zou J L, Ha N, Xiao R S, et al. Interaction between the laser beam and keyhole wall during high power fiber laser keyhole welding [J]. *Optics Express*, 2017, 25(15): 17650-17656.
- [24] Fabbro R, Slimani S, Coste F, et al. Study of keyhole behaviour for full penetration Nd-YAG CW laser welding [J]. *Journal of Physics D*, 2005, 38(12): 1881-1887.
- [25] Zou J L, Wu S K, Yang W X, et al. A novel method for observing the micro-morphology of keyhole wall during high-power fiber laser welding [J]. *Materials & Design*, 2016, 89: 785-790.
- [26] Zou J L, Wu S K, He Y, et al. Distinct morphology of keyhole wall during high power fibre laser deep penetration welding [J]. *Science and Technology of Welding and Joining*, 2015, 20(8): 655-658.
- [27] Zhang G L, Zhu B Q, Zou J L, et al. Correlation between the spatters and evaporation vapor on the front keyhole wall during fiber laser keyhole welding [J]. *Journal of Materials Research and Technology*, 2020, 9(6): 15143-15152.
- [28] Semak V, Matsunawa A. The role of recoil pressure in energy balance during laser materials processing [J]. *Journal of Physics D*, 1997, 30(18): 2541-2552.
- [29] Li M, Xiao R S, Zou J L, et al. Correlation between plume fluctuation and keyhole dynamics during fiber laser keyhole welding[J]. *Journal of Laser Applications*, 2020, 32(2): 022010.
- [30] Kaplan A F H. Fresnel absorption of 1 μm - and 10 μm -laser beams at the keyhole wall during laser beam welding: comparison between smooth and wavy surfaces[J]. *Applied Surface Science*, 2012, 258(8): 3354-3363.
- [31] Han X, Zhao Y, Zou J L, et al. Analysis of plume formation reasons in laser deep penetration welding based on visual observation [J]. *Chinese Journal of Lasers*, 2020, 47(6): 0602004.
韩雪, 赵宇, 邹江林, 等. 基于可视化观察的光纤激光深熔焊接羽辉形成原因分析[J]. *中国激光*, 2020, 47(6): 0602004.
- [32] Zou J L, Yang W X, Wu S K, et al. Effect of plume on weld penetration during high-power fiber laser welding[J]. *Journal of Laser Applications*, 2016, 28(2): 022003.

Spatter Characteristics of High-Power Fibre Laser Deep Penetration Welding and Effect of Defocus on Spatter

Zhang Gaolei, Kong Hua, Zou Jianglin^{*}, Zhao Zhenjia, Xiao Rongshi

High-Power and Ultrafast Laser Manufacturing Lab, Faculty of Materials and Manufacturing, Beijing University of Technology, Beijing 100124, China

Abstract

Objective Because of its high power, flexibility, compact size, and low operating cost, high-power fibre lasers have sparked widespread interest in laser welding. However, because of the high energy density of high power fibre lasers, producing a large number of spatter particles during welding is easy, which has a serious negative impact on welding. On the one hand, spatters will pollute the focusing mirror or be located in the laser beam transmission path, resulting in a change in the focusing characteristics of the laser beam and a loss of laser energy transmission, which will seriously affect the welding process's stability; on the other hand, spatters will cause weld metal loss, resulting in welding defects such as depression and incomplete weld. As a result, studying spatter generation is crucial for understanding the physical process of high power fibre laser welding and optimising welding technology.

Methods In this paper, a high-speed camera was used to observe the formation of spatters and the fluctuation behaviour of the molten pool during high-power fibre laser welding. The dimension and quantity of spatter were measured after welding using a scanning electron microscope, and the plate mass loss before and after welding was calculated. The power density of the fibre laser was altered by adjusting the defocus, and the number of spatters and plate mass loss were investigated. Finally, the effect of defocus on mass loss and spatter formation is investigated using the experimental results.

Results and Discussions The formation of typical spatter particles in fibre laser deep penetration welding was observed using a high-speed camera (Fig. 2). The spatter particles collected from the glass cylinder after welding were measured using a scanning electron microscope. The results show that the spatter particles were mostly distributed in the $>50\text{--}100\ \mu\text{m}$ range (Fig. 3). The relationship between plate mass loss and spatter number was then established, and the variation of spatter number and plate mass loss with defocus was demonstrated (Fig. 6). Finally, the spatter was related to the inclination angle of the front keyhole wall, the laser-induced vapour on the front keyhole wall, and the surface tension of the molten pool; the reason why the number of spatters increased with defocus was summarised.

Conclusions The spatter behaviour and effect of defocus in high power fibre laser deep penetration welding are investigated in this paper through *in-situ* optical observation of the molten pool and measurement of plate mass loss. The results show that the formation of spatter in fibre laser molten pool can be divided into three steps: molten pool bulges on the edge of keyhole \rightarrow the bulge is elongated to form a liquid column \rightarrow the liquid column breaks up to overcome the surface tension and form spatter particles. The spatter particles are mainly distributed between 50 and 100 μm . With the increase in laser defocus, the spatter number, plate mass loss and weld width gradually increase, whereas the penetration gradually decreases. Further investigation reveals that the eruption of spatters is related to the inclination angle of the front keyhole wall, impact force of laser-induced evaporation of the front keyhole wall, and molten pool surface tension. Increasing the defocus reduces the inclination angle of the front keyhole wall and the surface tension of the molten pool, which increases the impact force of the evaporation vapour from the front wall to the upper edge of the rear keyhole wall, resulting in more spatters.

Key words laser technique; spatter; molten pool; vapor; defocus; front keyhole wall

OCIS codes 140.3380; 160.3900; 140.3390